npj | computational materials

Article

Published in partnership with the Shanghai Institute of Ceramics of the Chinese Academy of Sciences

https://doi.org/10.1038/s41524-025-01922-w

High-efficiency computational methodologies for electronic properties and structural characterization of Ge-Sb-Te based phase-change materials

Shanzhong Xie, Kan-Hao Xue ✉, Shaojie Yuan, Zijian Zhou, Shengxin Yang, Heng Yu, Rongchuan Gu, Ming Xu ✉ & Xiangshui Miao

Theoretical simulation of phase change materials such as Ge-Sb-Te has suffered from two methodological issues. On the one hand, there is a lack of efficient band gap correction method for density functional theory that is suitable for these materials in both crystalline and amorphous phases, while maintaining the computational complexity comparable to local density approximation. On the other hand, analysis of the coordination number in amorphous phases relies on an integration involving the radial distribution function, which adds to the complexity. In this work, we find that the shell DFT-1/2 method offers overall band gap accuracy for phase-change materials comparable to that of the HSE06 hybrid functional, while its computational cost is orders of magnitude lower. Moreover, the mixed length-angle coordination number theory enables calculating the coordination numbers in the amorphous phase directly from the structure, with definite outcomes. The two methodologies could be helpful for high-throughput simulations of phase change materials.

Chalcogenide-based phase change materials (PCMs), especially Ge-Sb-Te (GST) alloys, have garnered significant attention for applications in both optical storage and non-volatile electronic memory[1–5]. Alloys in the pseudo-binary line of GeTe-Sb_2Te_3 exhibit rapid switching speeds, with various compositions exemplified by $Ge_1Sb_4Te_7$ (GST-147), $Ge_1Sb_2Te_4$ (GST-124), $Ge_2Sb_2Te_5$ (GST-225) and $Ge_3Sb_2Te_6$ (GST-326). From GST-326 to GST-147, the switching speed gradually increases, but the corresponding stability of the amorphous phase degrades, and the crystallization temperature T_x decreases to 85 °C[6]. Theoretical simulations of PCMs mainly involve the dynamics of the phase change process and the electronic structure. For the former, the microscopic mechanisms pertaining to the nucleation and growth processes should be emphasized, with ab initio molecular dynamics (AIMD) as the core technique. The mechanisms that drive the phase transitions and the large resistivity differences between the crystalline and amorphous phases are still under intensive investigation. The latter task, studying the electronic structure from first principles, could serve as a foundation for understanding the physical properties of PCMs. The band gaps of both amorphous and crystalline phases, along with trap states, remain central topics of investigation.

Density functional theory (DFT)[7,8] has become the mainstream theoretical method to study the electronic structure of solids. Although DFT suffers from inaccuracies in exchange and correlation terms, it is significantly more efficient than post-Hartree-Fock quantum chemistry methods and is suitable for studying PCMs, which typically require large unit cells. Existing DFT studies have provided in-depth atomic-scale understanding of the characteristics of GST compounds, especially GST-225. It is known that stable crystalline phases of GST are in either $P\bar{3}m1$ or $R\bar{3}m$ symmetries, where Ge, Sb, and Te atoms are stacked sequentially along the c-axis. Yet, the exact features of their electronic structures are still subject to intensive discussions[9–12]. Accurate theoretical calculations on the entire series of GST compounds should help clarify these issues. Nevertheless, DFT significantly underestimates band gaps when using the standard local density approximation (LDA)[13,14] and generalized gradient approximation (GGA)[15–17]. Two typical solutions are the hybrid functional scheme[18–20] and the quasi-particle-based GW approximation[21–23]. These advanced approaches, particularly the HSE06 hybrid functional, have been widely employed in the electronic structure study of phase-change materials[24–29]. Although these methods effectively address the band gap issue, they inevitably introduce an increase in computational load. While hybrid functionals are feasible with local bases, it becomes much heavier together with the plane wave basis set. Accordingly, there remains a need for a band gap correction method with computational complexity comparable to that of LDA[30]. The

School of Integrated Circuits, Huazhong University of Science and Technology, Wuhan, 430074, China. ✉e-mail: xkh@hust.edu.cn; mxu@hust.edu.cn

DFT-1/2 method, introduced by Ferreira et al.[31,32], and its variant, the shell DFT-1/2 method developed in refs. 33–36, provide another route that only uses the self-energy potentials to correct the self-interaction errors due to LDA and GGA. In particular, shell DFT-1/2 accurately reproduces the electronic band structure of Ge[33], without relying on empirical parameters, and demonstrates excellent band gap accuracy in Sb-based semiconductor superlattices used for infrared detection[37]. Recently, it has also been successfully applied to perovskite $BaBiO_3$ to capture light-induced insulator-to-metal transition via nonlinear phononics[38]. The computational speed of shell LDA-1/2 (where LDA is used for the exchange-correlation term in DFT) is comparable to that of conventional LDA[39], and is sometimes even faster[34], as the removal of unphysical electron self-interaction can accelerate the convergence of the self-consistent cycle. However, shell DFT-1/2 has not yet been applied to the calculation of GST compounds.

A distinctive characteristic of PCMs is their inherent nature as narrow-gap semiconductors, which poses significant challenges for the precise determination and theoretical reproduction of their electronic structures. For instance, consider a computational method that could predict the band gaps of a certain type of semiconductors with an absolute error of ~0.5 eV. While such predictive accuracy seems to be acceptable for a wide gap semiconductor (such as Ga_2O_3 with a ~4.9 eV gap) or an insulator (such as HfO_2 with a ~5.9 eV gap), it may be insufficient for materials with narrower band gaps or more complex electronic structures (e.g., the band gaps of PCMs typically lie below 0.6 eV). Moreover, PCMs usually show a strong spin-orbit coupling (SOC) effect. For example, GST comprises a high proportion of heavy elements, such as Sb and Te. The works by Lawal et al.[40] and Hsieh et al.[41] show that, Sb_2Te_3 is a topological insulator hosting gapless surface states, thanks to its strong SOC effect and time-reversal symmetry protection. When the SOC effect is taken into account, the calculated band gaps are expected to be lower than those obtained without SOC.

It is sometimes tempting to believe that the systematic band gap underestimation by LDA/GGA could be compensated by band gap enhancement through neglecting the SOC effect. In the literature, such calculations are commonplace, and indeed some calculated band gaps appear reasonable. Lee and Jhi obtained a 0.26 eV band gap for crystalline GST-225 using GGA[9]. Yamanaka et al.[10] studied both the cubic and the hexagonal phases of GST-225 using LDA, and obtained a 0.1 eV band gap for the former, while the latter phase showed no band gap in the calculation. Park et al.[11] calculated the electronic structures of GeTe, GST-147, GST-124, GST-225 as well as Sb_2Te_3, and the band gaps were, respectively, 0.66 eV, 0.34 eV, 0.43 eV, 0.41 eV, and 0.17 eV given by the Perdew-Burke-Ernzerhof (PBE) functional[16]. Ibarra-Hernández et al.[12] obtained 0.225 eV and 0.25 eV band gaps for GST-124 and GST-225, respectively, using the PBEsol (a solid-state version of PBE) functional[42]. Their calculation predicted GST-326 to be metallic with a zero band gap.

These results above show that it is possible to obtain acceptable band gaps using conventional GGA while neglecting SOC, though in some cases it may fail to predict a finite band gap. Nevertheless, this scheme could be recommended only if the band gap underestimation by GGA is exactly offset by the SOC-induced gap shrinkage. Unfortunately, they come from very distinct origins. The SOC effect is more severe for compounds with heavier elements, but the intrinsic gap underestimation by GGA is not relevant to the nature of light or heavy elements. Hence, the compositional ratio of GeTe to Sb_2Te_3 ought to impact the amount of SOC-induced band gap reduction, thus conventional LDA/GGA alone is not supposed to predict reliable band gaps for the entire series of GST. In fact, even for the extensively studied GST-225, achieving a quantitatively accurate band gap is challenging when SOC is considered, particularly when the computational complexity is maintained at the LDA/GGA level.

To sum up, the theoretical understanding of GST's electronic structure is hampered by a triple challenge: (i) the inherent band gap underestimation of standard DFT, (ii) the significant and composition-dependent SOC effects that must be included for physical correctness, and (iii) the computational inefficiency of using advanced methods like *GW* for systematic studies. The common compromise of using GGA without SOC is empirically inconsistent and physically unsound. Therefore, there is a definite need for a computational framework that simultaneously addresses the exchange-correlation error and the SOC effect, while retaining the efficiency of standard DFT.

This work, therefore, aims at exploring the computational method that is capable of recovering the band gaps of PCMs exemplified by GST, considering SOC but keeping the computational load at the same level of LDA/GGA. Our study focuses on the pseudo-binary line of GeTe-Sb_2Te_3, including their parent compounds (Sb_2Te_3 and GeTe) and representative GST compositions such as GST-124, GST-147, GST-225, and GST-326. The electronic structures of both crystalline and amorphous phases are investigated. The shell GGA-1/2 method with SOC (shGGA-1/2 + SOC for short) demonstrates high efficiency, and is compared with GGA, GGA + SOC, shGGA-1/2, HSE06[20,43,44], HSE06 + SOC, SCAN[45], SCAN + SOC, mBJ[46,47], and mBJ+SOC. Moreover, for coordination number analysis, we have found that the mixed length-angle coordination number theory (MLAC)[48] is particularly suitable for PCMs.

Results and discussion

Crystalline phase: band structure analysis

The electronic band structures for the crystalline models are illustrated in Figs. 1–3 as well as in Table 1, using GGA, GGA + SOC, shGGA-1/2, shGGA-1/2 + SOC, HSE06, and HSE06 + SOC respectively (see Methods section for details). Other band structure results, as obtained by SCAN[45], SCAN + SOC, mBJ[46,47], mBJ+SOC are presented in Figs. S10 and S11. Using conventional GGA (Fig. 1a–f), Sb_2Te_3 is shown to possess a direct 0.18 eV band gap, with the valence band maximum (VBM) and conduction band minimum (CBM) both lying at Γ. GST-147 shows a 0.24 eV direct gap, with both VBM and CBM located at A. Near Γ, however, GST-147 has two valleys for the conduction band, whose energies are almost degenerate with the Γ point (differing by merely 0.02 eV). For GST-124 and GST-225, GGA predicts indirect gaps. Their VBMs both lie at Γ, and the CBMs are close to Γ. The magnitudes of GGA gaps are 0.35 eV and 0.24 eV, respectively. GST-326 is predicted to possess a direct Γ—Γ gap of 0.29 eV. In GeTe, the VBM is along the Γ—L line, while the CBM is very close to the T point. The indirect gap value is 0.54 eV as predicted by standard GGA.

When SOC is turned on, it follows from Fig. 1g–l that all band gaps become less than 0.1 eV, except for GeTe. Moreover, in GST-147, the type of band gap changes from direct to indirect. However, GST-124 and GST-225 manifest direct gaps after SOC is considered, though they were predicted as direct semiconductors under GGA without SOC. Note that these materials possess narrow gaps, and in each case the difference between direct and indirect gaps is not prominent. Hence, it is difficult to precisely judge the type of band gaps from experimental data, and there are few published measurements of gap types. Accordingly, the magnitude of band gap should be our primary focus here, though there are clues from our theoretical calculations that turning on SOC could change the type of gap in GST.

Both the self-energy correction method shGGA-1/2 and the hybrid functional HSE06 are very effective in rectifying the band gap problem of GGA. Figures 2 and 3 show the shGGA-1/2 and HSE06 results, respectively, either without or with SOC turned on. In the absence of SOC effect, the predicted gap values in (shGGA-1/2, HSE06) format are Sb_2Te_3 (0.67 eV, 0.87 eV), GST-147 (0.89 eV, 0.87 eV), GST-124 (0.95 eV, 0.98 eV), GST-225 (0.89 eV, 0.83 eV), GST-326 (0.90 eV, 0.87 eV) and GeTe (1.43 eV, 1.39 eV). The shGGA-1/2 values are all close to HSE06 values, even though shGGA-1/2 is computationally much lighter. Considering the SOC effect, however, the band gaps are predicted to be Sb_2Te_3 (shGGA-1/2: 0.27 eV, HSE06: 0.51 eV), GST-147 (0.45 eV, 0.42 eV), GST-124 (0.59 eV, 0.58 eV), GST-225 (0.57 eV, 0.54 eV), GST-326 (0.61 eV, 0.63 eV), GeTe (1.31 eV, 1.21 eV). The only big discrepancy between shGGA-1/2 and HSE06 occurs in the case of Sb_2Te_3, but the shGGA-1/2 gap is closer to experimental. The SOC effect also has a great impact in shGGA-1/2 and HSE06 calculations. For Sb_2Te_3 and GeTe, shGGA-1/2 + SOC predicts a 0.27 eV direct gap and a 1.31 eV indirect gap, respectively. The result for Sb_2Te_3 is consistent with a *GW* calculation by Lawal et al.[49] (0.22 eV). Without considering SOC, the

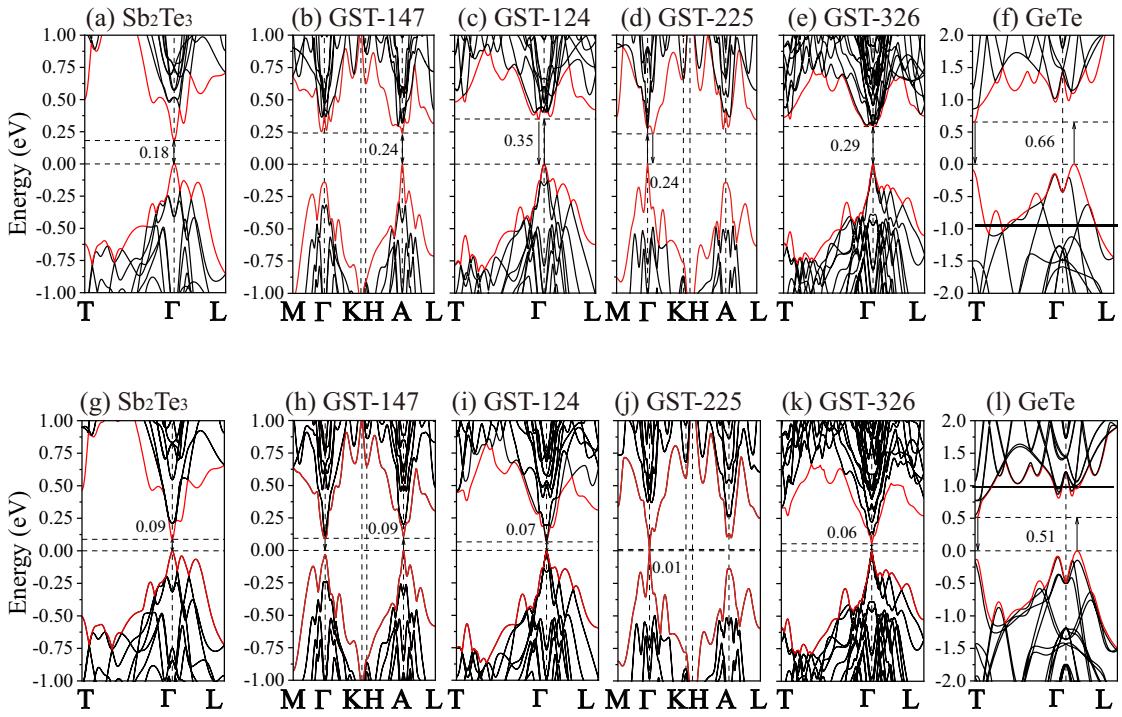

Fig. 1 | Energy band diagrams calculated using GGA. **a** Sb_2Te_3 without SOC; **b** GST-147 without SOC; **c** GST-124 without SOC; **d** GST-225 without SOC; **e** GST-326 without SOC; **f** GeTe without SOC; **g** Sb_2Te_3 with SOC; **h** GST-147 with SOC; **i** GST-124 with SOC; **j** GST-225 with SOC; **k** GST-326 with SOC; **l** GeTe with SOC.

Table 1 | Calculated and experimental band gaps

	Band gap (eV)					
	Sb_2Te_3	GST-147	GST-124	GST-225	GST-326	GeTe
E_g^{GGA}	0.18 (*d*)	0.24 (*d*)	0.35 (*d*)	0.24 (*i*)	0.29 (*i*)	0.66 (*i*)
$E_g^{GGA+SOC}$	0.09 (*d*)	0.09 (*i*)	0.07 (*d*)	0.01 (*d*)	0.06 (*d*)	0.51 (*i*)
$E_g^{shGGA-\frac{1}{2}}$	0.67 (*d*)	0.89 (*d*)	0.95 (*d*)	0.89 (*d*)	0.90 (*d*)	1.43 (*i*)
$E_g^{shGGA-\frac{1}{2}+SOC}$	0.27 (*d*)	0.45 (*d*)	0.59 (*d*)	0.57 (*d*)	0.61 (*d*)	1.31 (*i*)
E_g^{HSE06}	0.87 (*d*)	0.87 (*i*)	0.98 (*i*)	0.83 (*i*)	0.87 (*d*)	1.39 (*i*)
$E_g^{HSE06+SOC}$	0.51 (*d*)	0.42 (*d*)	0.58 (*d*)	0.54 (*d*)	0.63 (*d*)	1.21 (*i*)
E_g^{SCAN}	0.18 (*d*)	0.19 (*i*)	0.28 (*i*)	0.15 (*i*)	0.19 (*i*)	0.66 (*i*)
$E_g^{SCAN+SOC}$	0.13 (*d*)	0.07 (*i*)	0.02 (*d*)	0.10 (*d*)	0.03 (*d*)	0.51 (*i*)
E_g^{mBJ}	0.44 (*d*)	0.34 (*d*)	0.42 (*i*)	0.30 (*d*)	0.42 (*i*)	0.79 (*i*)
$E_g^{mBJ+SOC}$	0.07 (*d*)	0.04 (*d*)	0.01 (*d*)	0.05 (*d*)	0.11 (*d*)	0.67 (*i*)
Experimental	0.15—0.22[80]	-	0.55[11]	0.57[11] 0.5[81]	-	0.61[11]

The band gap values and types for the six materials (Sb_2Te_3, GST-147, GST-124, GST-225, GST-326, and GeTe), as obtained using different computational methods, are summarized, where "d" and "i" denote direct and indirect band gaps, respectively.

shGGA-1/2 gap of Sb_2Te_3 is 0.67 eV, thus the SOC-induced gap shrinkage is as large as 0.4 eV. The strong SOC effect observed in Sb_2Te_3 agrees with the experimental results[40,41].

The shGGA-1/2 + SOC band gap for GeTe (1.31 eV) is much greater than experimentally reported 0.61 eV. Note that the HSE06 + SOC gap (1.21 eV) is also large. A possible reason is that practical GeTe samples are populated with Ge vacancies[50,51], and sometime with Te vacancies as well. A Ge vacancy could include a filled state within the forbidden band, and the observed excitation starting from this state may need less energy for the electron to reach the conduction band.

With more GeTe contained in GST, it is discovered that the shGGA-1/2 + SOC gaps show an increasing trend, which is consistent with the experimental results of Park et al.[11]. A comparison of shGGA-1/2 + SOC gaps with typical experimental gaps is in general satisfactory: GST-225 (shGGA-1/2 + SOC: 0.57 eV, experimental: 0.57 eV); GST-147 (shGGA-1/2 + SOC: 0.59 eV, experimental: 0.55 eV). A benchmark for GST-326 is not yet possible due to a lack of experimental data. In addition, since Te is the heavier anion element in GST, it is supposed that the effect of SOC will be more severe for GST with more Te content. As shown in Table 2, both shGGA-1/2 and HSE06 calculations follow this trend exactly. This is verified by computing $E_g - E_g^{SOC}$, where a larger difference indicates a stronger SOC effect. Nevertheless, plain GGA calculations do not follow this trend, possibly due to the over-narrow gap nature in this series of compounds. This also confirms the point that, GGA-induced gap underestimation cannot simply compensate the SOC-induced gap variation in GST, because the two mechanisms intrinsically have very different origins. Provided that the HSE06 + SOC results are regarded as the reliable standards, then through inspecting $E_g^{GGA+SOC} - E_g^{HSE06+SOC}$, one could find that (i) GGA + SOC leads to very inaccurate band gap values; (ii) GGA + SOC does not show a consistent trend across the GST compositions, since GST-147 behaves quite differently compared with other compounds. On the contrary, $E_g^{shGGA-\frac{1}{2}+SOC} - E_g^{HSE06+SOC}$ shows a very consistent trend (also shown in Table 2).

Efficiency and accuracy comparison

While similar in electronic structure accuracy, the computational efficiencies of shGGA-1/2 and HSE06 differ much. To quantify this difference fairly, we compared the computational time of all ten methods (GGA, GGA + SOC, shGGA-1/2, shGGA-1/2 + SOC, HSE06, HSE06 + SOC, SCAN, SCAN + SOC, mBJ, mBJ+SOC) across the selected PCMs. Usually, less *k* points have to be used in HSE06 calculations, but GGA, shGGA-1/2, SCAN, and mBJ permit more *k* points within a reasonable time frame. This inevitably causes an unfair comparison if only the total time is recorded.

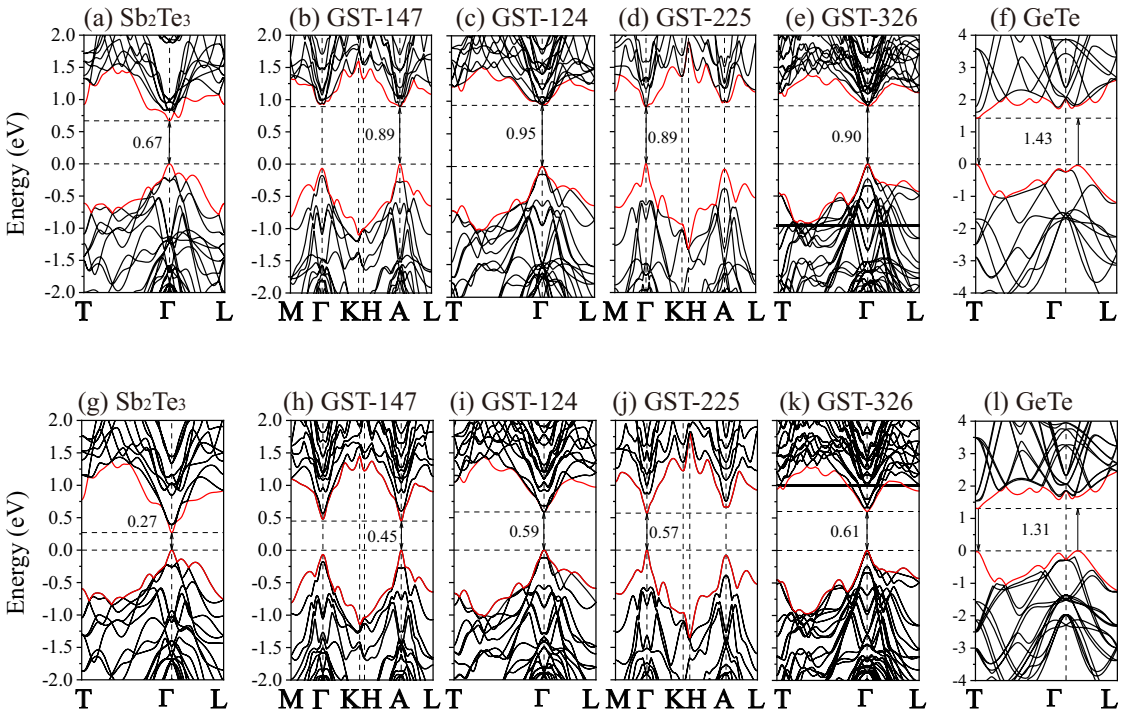

Fig. 2 | Energy band diagrams calculated using shGGA-1/2. a Sb_2Te_3 without SOC; **b** GST-147 without SOC; **c** GST-124 without SOC; **d** GST-225 without SOC; **e** GST-326 without SOC; **f** GeTe without SOC; **g** Sb_2Te_3 with SOC; **h** GST-147 with SOC; **i** GST-124 with SOC; **j** GST-225 with SOC; **k** GST-326 with SOC; **l** GeTe with SOC.

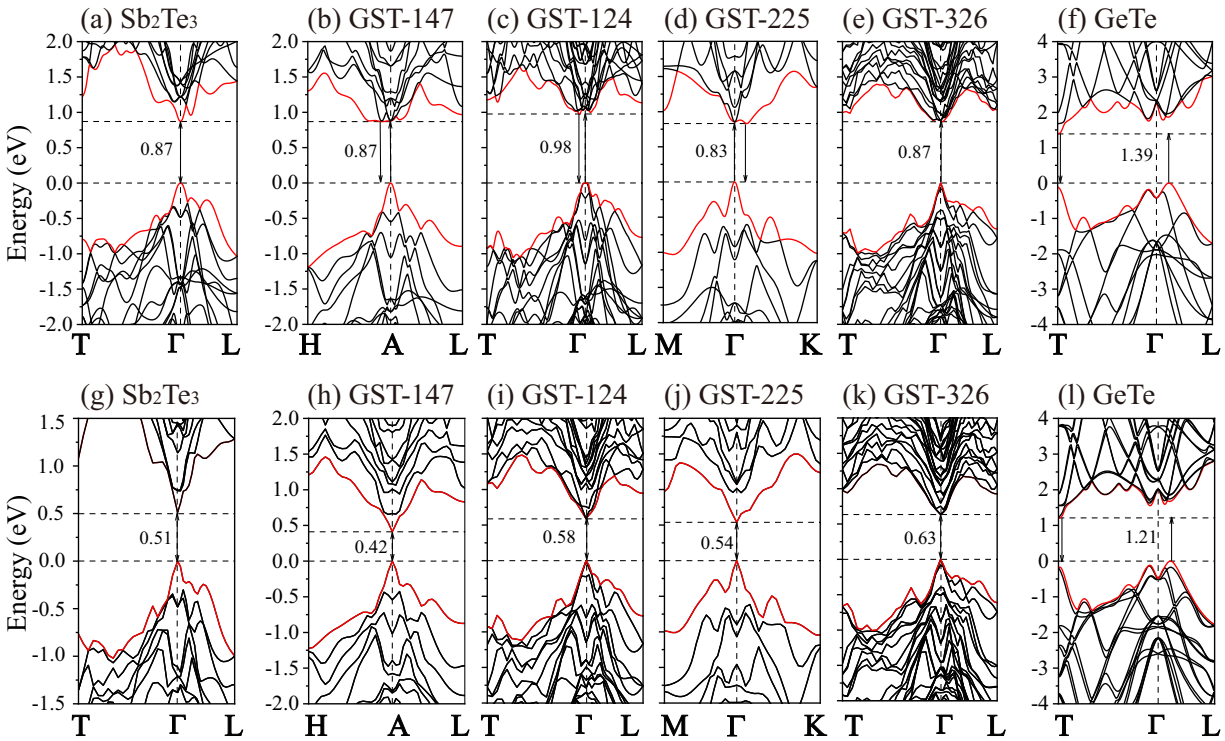

Fig. 3 | Energy band diagrams calculated using the HSE06 hybrid functional. **a** Sb_2Te_3 without SOC; **b** GST-147 without SOC; **c** GST-124 without SOC; **d** GST-225 without SOC; **e** GST-326 without SOC; **f** GeTe without SOC; **g** Sb_2Te_3 with SOC; **h** GST-147 with SOC; **i** GST-124 with SOC; **j** GST-225 with SOC; **k** GST-326 with SOC; **l** GeTe with SOC.

Table 2 | Impact of SOC on the band gaps of the crystalline GST samples

	GST-326	GST-225	GST-124	GST-147
Te content	54.5%	55.6%	57.1%	58.3%
$E_g^{GGA} - E_g^{GGA+SOC}$ (eV)	0.23	0.23	0.28	0.15
$E_g^{shGGA-\frac{1}{2}} - E_g^{shGGA-\frac{1}{2}+SOC}$ (eV)	0.29	0.32	0.36	0.44
$E_g^{HSE06} - E_g^{HSE06+SOC}$ (eV)	0.24	0.29	0.40	0.45
$E_g^{GGA+SOC} - E_g^{HSE06+SOC}$ (eV)	−0.57	−0.53	−0.51	−0.33
$E_g^{shGGA-\frac{1}{2}+SOC} - E_g^{HSE06+SOC}$ (eV)	−0.02	0.03	0.01	0.03

This table presents data on the influence of spin-orbit coupling (SOC) for four crystalline GST compounds (GST-326, GST-225, GST-124, GST-147). It lists the Te content for each compound and provides the calculated differences in band gaps between computational methods with and without SOC (GGA, shGGA-1/2, HSE06), as well as the differences between the results of selected methods when SOC is included.

Table 3 | Average time costs for one irreducible *k*-point in each method

	Time (second)					
	Sb_2Te_3	GST-147	GST-124	GST-225	GST-326	GeTe
GGA	0.7	1.0	1.2	0.4	3.5	0.1
GGA + SOC	1.1	1.7	4.1	0.4	11.4	0.2
shGGA-1/2	0.7	1.2	1.2	0.4	3.5	0.1
shGGA-1/2 + SOC	1.1	2.0	4.0	0.5	13.2	0.2
HSE06	2380	1875	5063	5879	7643	108.7
HSE06 + SOC	7392	6379	5023	1827	14646	477.7
SCAN	4.5	27.7	4.8	1.1	6.0	0.4
SCAN + SOC	16.0	10.0	36.3	4.9	44.7	1.5
mBJ	22.5	14.7	38.7	6.0	169.2	3.1
mBJ+SOC	60.0	84.0	271.6	42.0	332.4	13.5

This table lists the average computational time cost, in seconds, required to process one irreducible k-point for each of the six materials (Sb_2Te_3, GST-147, GST-124, GST-225, GST-326, GeTe) across various methods, including GGA, shGGA-1/2, HSE06, SCAN, mBJ and their respective versions with spin-orbit coupling (SOC) included.

Hence, we re-did the GGA, shGGA-1/2, SCAN, and mBJ calculations using the same *k*-point meshes as employed in their corresponding HSE06 calculations. Detailed *k*-point information for all test cases is provided in Supplementary Note 1 and Supplementary Table 1. For a few particularly demanding HSE06 + SOC cases, slightly sparser *k*-meshes were unavoidable. Furthermore, recognizing that each material possesses a specific number of irreducible *k*-points, we emphasize the average computational time per irreducible *k*-point as the most consistent metric for cross-method comparison. These data are summarized in Table 3, while the total computational times and the corresponding numbers of irreducible *k*-points are listed in Supplementary Table 2 and Supplementary Table 3.

The recorded computational times correspond to the second step involving self-consistent band structure calculations, where the initial wavefunction files were all obtained from the first-step PBE self-consistent calculations. For band structure calculations using the mBJ functional, we used an additional self-consistent step to determine the mBJ *c* parameters required for the calculation, though the wavefunction file for the second-step band structure calculation still originated from the initial PBE self-consistent step. All calculations were performed on a Linux server possessing 128 cores, with consistent parallelization parameters (parallelization in 8 groups, and 16 bands optimized at a time). The results clearly demonstrate that shGGA-1/2 exhibits computational speed comparable to conventional GGA, regardless of whether SOC is included.

Crystalline phase: coordination number analysis

In characterizing the local structure in GST, the distribution of Sb-Te bond lengths usually shows two peaks at around 2.97 Å and 3.17 Å[52–54]. Coordination number (CN) for an atom/ion in a solid has traditionally been determined according to the lengths of its bonds. This method has certain limitations in case the bond length distribution is not sharply divided into short and long classes. Although the 0.2 Å difference in the bond lengths of crystalline GST does not cause confusion, identifying the CN in amorphous GST cannot simply rely on the bond length analysis, but it requires an integration taking advantage of the pair correlation function. Recently, we have proposed a CN theory based on both the bond lengths and bond angles, which may be called the mixed length-angle coordination (MLAC)[48]. This theory also lists the bond lengths in ascending order, but whether a new bond is counted in the coordination depends on its angles to existing bonds. If it makes an angle greater than θ=65° with respect to any of the existing bonds, then it is counted. Otherwise, the counting stops. Detailed explanation of the MLAC theory is given in the original publication[48], as well as in Supplementary Note 2 of this work. Using the MLAC method, we find that the CNs of Ge or Sb are always 6 in the six materials under investigation, but the CNs of Te differ. According to the data shown in Supplementary Table 4, three distinct Te sites can be identified. Te1 represents a Te atom with 6-coordination (6C), which only has bonds with Ge, or only with Sb. Te2 is a different Te site that is 6C, but it possesses Ge-Te bonds and Sb-Te bonds, simultaneously. Te3 is a 3C Te site connected only to Sb atoms. Detailed information regarding the coordination configurations in the six materials can be found in Supplementary Note 3.

As demonstrated in Supplementary Table 7, there are two sorts of Sb-Te bonds in Sb_2Te_3 and the various GST models. In GST, the bond lengths are 2.99 Å and 3.15 Å, respectively. In Sb_2Te_3 the bonds are slightly longer, but with the same trend discovered. In GeTe, there are two distinct Ge-Te bond lengths as well. This fact is consistent with many reports in the literature. For example, based on ab initio Raman spectra, Sosso et al. revealed that Sb_2Te_3 contains two Sb-Te bond length values of 2.97 Å and 3.17 Å[52]. Kolobov et al. revealed from extended X-ray absorption fine structure spectroscopy that there are two sorts of Sb-Te bond lengths in GST-225, with values of 2.83 Å and 3.15 Å, respectively[53]. Experimental studies have also reported that GeTe has two bond lengths, 2.80 Å and 3.13 Å[53,54]. In addition, for a 6C Sb atom in GST or Sb_2Te_3, its six bonds can be divided into 3 short bonds and 3 long bonds. A short bond involves bonding to a 3C Te atom (i.e., Te3), while a long bond involves bonding to a 6C Te atom (i.e., Te1 or Te2).

Amorphous phase: electronic structure analysis

The amorphous models for the six materials are demonstrated in Fig. 4 as well as Supplementary Table 8. These models were generated through AIMDs (see "Methods" section for details). The lattice parameters and theoretical number densities are taken from the fully relaxed structures, though the initial structures are metastable cubic GST. In such an initial structure, Te atoms constitute a sub-lattice of the rock salt structure, while Ge, Sb, and vacancies are randomly distributed on the other sub-lattice[55–57]. The exact composition used for each model in the cubic crystalline cell and the theoretical number densities of the models after full relaxation are shown in Supplementary Table 8. The total number of atoms in a supercell ranges from 270 to 300. The theoretical atomic number densities range between 0.0272 $Å^{-3}$ and 0.0310 atoms $Å^{-3}$, close to the experimental value (0.030 atoms $Å^{-3}$)[58]. At 300 K, the partial pair distribution functions $g(r)$ are shown in Supplementary Fig. 9. The definition of $g(r)$ and its calculation method are explained in Supplementary Note 4. Upon increasing the GeTe content in GST, the $g(r)$ peak corresponding to the Ge–Te bond becomes more pronounced, confirming the structural validity of the amorphous models. According to Fig. 4, no substantial de-mixing is observed, and all our generated amorphous models still represent homogeneous phases.

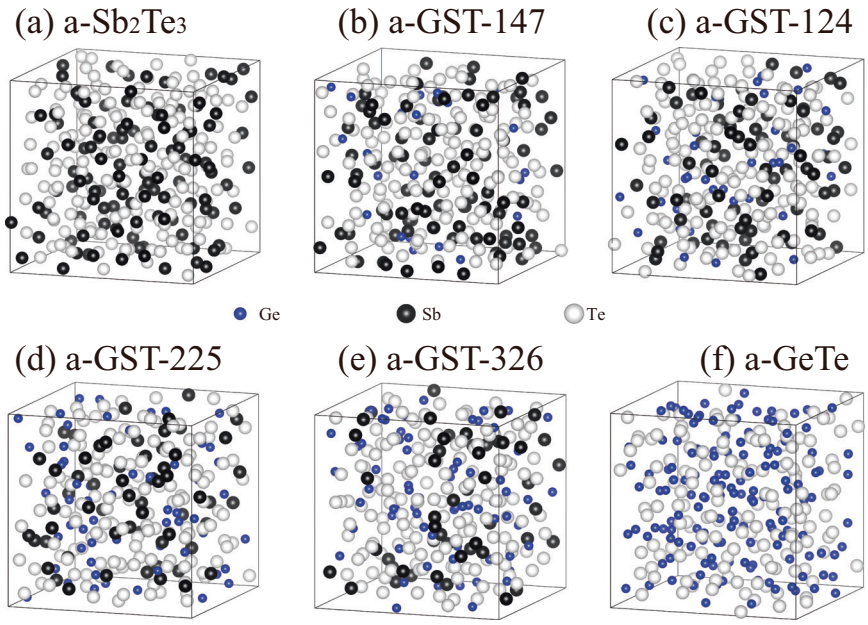

Fig. 4 | Model structures of amorphous GST-related compounds. **a** a-Sb_2Te_3; **b** a-GST-147; **c** a-GST-124; **d** a-GST-225; **e** a-GST-326; and **f** a-GeTe.

We subsequently calculated the electronic structures of these amorphous models using GGA, GGA + SOC, shGGA-1/2 as well as shGGA-1/2 + SOC. Hybrid functionals were not applied due to the high computational cost. We used the inverse participation ratio (IPR) to identify the mobility gaps and trap states—a methodology with broad applications in prior studies[59–61]. The definition of the mobility gap and the calculation method for IPR are given in Supplementary Note 5 and Supplementary Note 6. In general, larger IPR values indicate stronger localization of electron states. The mobility gaps (E_{gm}) of the amorphous models were obtained through calculating the energy separation between the mobility edges. For either the conduction band or the valence band, its mobility edge may be extracted with the assistance of IPR values[62].

The most common composition GST-225 is taken as our focus for analysis. As illustrated in Fig. 5, the roughly estimated E_{gm} values by GGA, GGA + SOC, shGGA-1/2 and shGGA-1/2 + SOC are 0.70 eV, 0.55 eV, 0.89 eV and 0.85 eV, respectively. All methods predict the presence of trap states. These trap states show large IPR values, indicating that the carriers trapped at these localized states will contribute little to the electrical conduction at room temperature because of the low mobility. It turns out that shGGA-1/2 could capture more gap states compared with GGA. Experimentally, Kato et al.[63] obtained a 0.74 eV Tauc gap for a-GST-225, and the energy width of the Urbach edge was ~0.2 eV (relative to the Fermi level, which was set to zero). They further pointed out that the exact location of the low-energy edge was unknown, and accordingly, the density of states around the VBM was vague. For sulfide and selenide glasses, it is known that the Tauc gap is smaller than the mobility gap and that the Urbach edge is governed by the valence-band tail[64]. Hence, the VBM should be lower than the Fermi level by at least 0.2 eV, according to experimental clues. And the mobility gap should be larger than 0.74 eV. In our calculation results, the distance of the Fermi level with respect to the lower edge of the mobility gap is indicated as A, B, C, and D in each case. The distance values are 0.14 eV (GGA), 0.18 eV (GGA + SOC), 0.15 eV (shGGA-1/2) and 0.22 eV (shGGA-1/2 + SOC), respectively. Of them, only that predicted by shGGA-1/2 + SOC is greater than 0.2 eV. The quality of shGGA-1/2 + SOC calculation has been demonstrated in terms of the band edge location, trap states, and the localization effect.

On account of the effectiveness of shGGA-1/2 + SOC in recovering the electronic structures of a-GST-225, we finished the calculations for other amorphous model structures. As shown in Fig. 6, the mobility gaps predicted by shGGA-1/2 + SOC for a-Sb_2Te_3, a-GST-147, a-GST-124, a-GST-326, and a-GeTe are 0.67 eV, 0.76 eV, 0.85 eV, 0.83 eV, and 0.88 eV, respectively, showing a consistent trend with the experimental mobility gap results by Park et al.[11].

Amorphous phase: coordination number analysis

Analysis of the CN in an amorphous structure is more challenging compared with crystalline phases. We first applied the traditional integration method using the radial distribution function, $RDF(r)$. The mathematical details of this method are given in Supplementary Note 4. Moreover, the CNs for the amorphous phases were also calculated within the MLAC context. Table 4 shows the average number of atoms in each specific CN, per supercell, for all six amorphous materials. The averaging was performed over 3000 AIMD steps, with a time interval of 2 fs. Additionally, we also recorded the MLAC information for three specific AIMD steps: the 1000th, 2000th, and 3000th steps, which are shown in Supplementary Table 10. The MLAC approach yields CN values that are slightly different from those obtained by the traditional method, but the overall trend remains consistent.

Discussion

We report two effective and efficient methods for analyzing the PCMs exemplified by GST. The shell GGA-1/2 method, a self-energy correction approach with LDA/GGA-level computational complexity, accurately reproduces the electronic structures of crystalline Sb_2Te_3 (predicted band gap: 0.27 eV), GST-147 (0.45 eV), GST-124 (0.59 eV), GST-225 (0.57 eV) and GST-326 (0.61 eV), particularly in terms of band gaps. In contrast, the plain GGA calculation could yield acceptable band gaps only if the SOC effect is neglected, but the impact of SOC is distinct in the entire series of GST compounds, which inevitably renders inconsistent physical results. Using the shell GGA-1/2 method with SOC correction, the calculated band gap of rhombohedral GeTe is 1.31 eV. While this result seems over-large, it demonstrates remarkable agreement with the more computationally demanding HSE06 + SOC calculation (1.21 eV). Notably, despite achieving comparable accuracy to the HSE06 functional, the shell GGA-1/2 approach exhibits superior computational efficiency, with a speed enhancement of nearly three orders of magnitude. Shell DFT-1/2 + SOC also predicts reasonable mobility gaps in amorphous GST (*e.g.*, a mobility gap of 0.81 eV for amorphous GST-225).

On the other hand, the MLAC theory has been shown to be suitable for analyzing the CNs in amorphous GST. While giving exactly identical CNs of crystalline GST as the traditional radial distribution function integration method, the new theory yields similar but not identical results for amorphous GST samples. The new method is efficient because it does not require

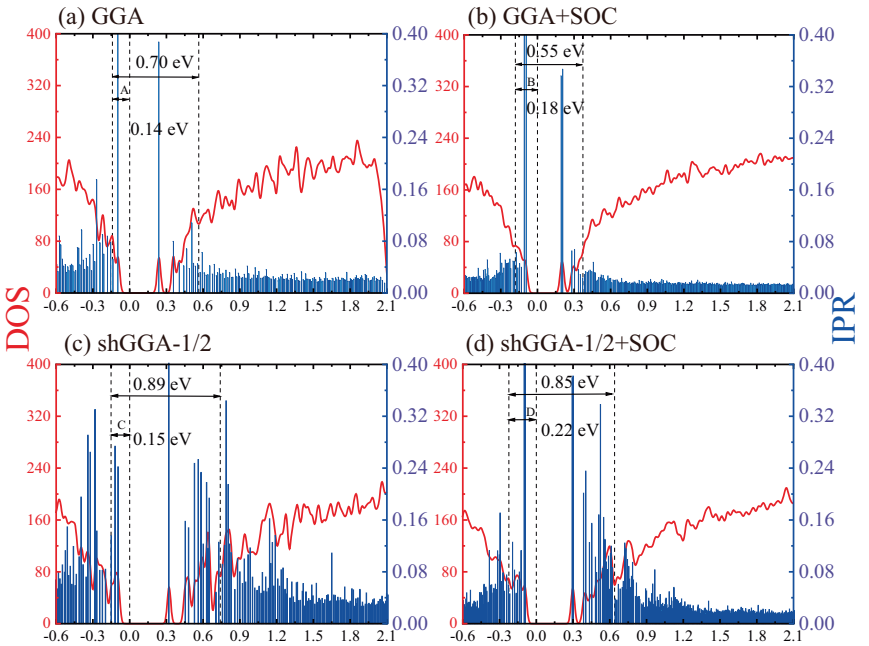

Fig. 5 | DOS and IPR of a-GST-225 under different computational methods. a GGA; **b** GGA + SOC; **c** shGGA-1/2; **d** shGGA-1/2 + SOC. The Fermi level corresponds to zero energy.

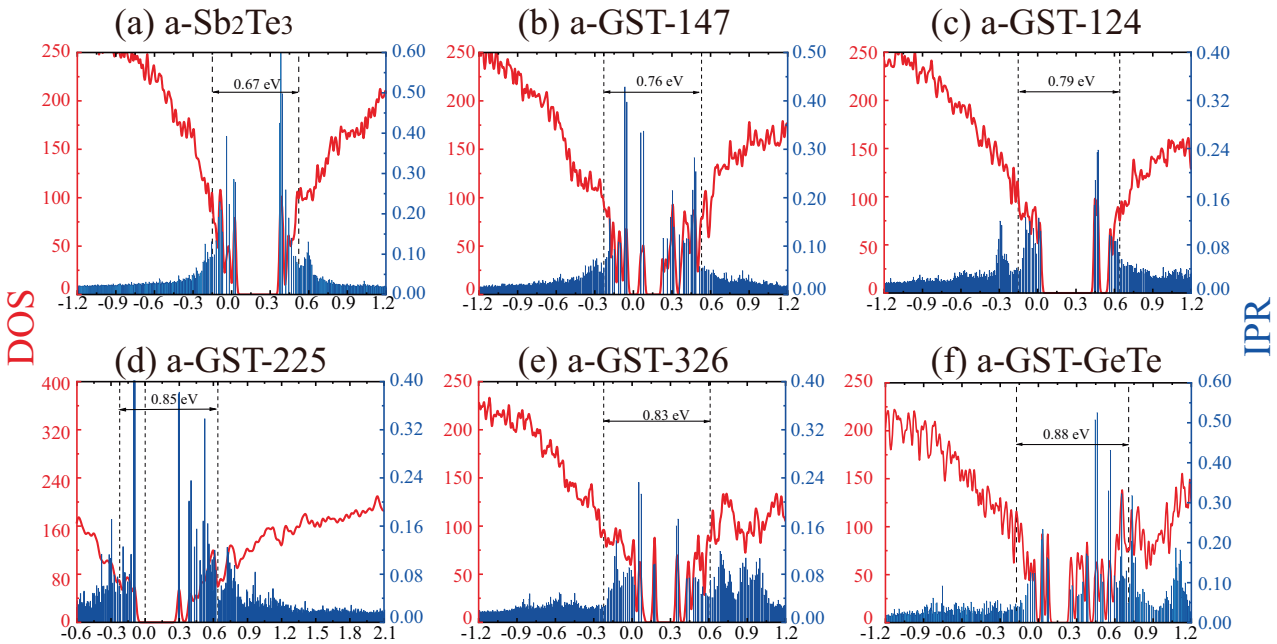

Fig. 6 | DOS and IPR of amorphous phase-change materials using shGGA-1/2 + SOC. a a-Sb_2Te_3; **b** a-GST-147; **c** a-GST-124; **d** a-GST-225; **e** a-GST-326; **f** a-GeTe. The Fermi level corresponds to zero energy.

any integration; the CN of a specified atom can be directly obtained by inspecting bond angles. This new perspective may enable more effective CN analysis in the amorphous phases of PCMs.

It is important to note that the crystalline structural models employed in this work are based on idealized, fully ordered stackings. We acknowledge that experimentally synthesized GST compounds, such as GST-225, GST-147, and GST-326, often exhibit varying degrees of cation disorder in the Ge/Sb sublattice, a fact well-documented in the literature[57,65–67]. This disorder is known to influence the electronic structure, particularly the band gap, as various stackings (e.g., Petrov vs. Kooi) can yield different theoretical band gaps. The primary objective of this study was to evaluate the performance of the shGGA-1/2 methodology against established benchmarks. Therefore, we utilized these well-defined, ordered models as a standardized and computationally tractable testbed. The remarkable agreement between our shGGA-1/2 + SOC results and HSE06 + SOC calculations, as well as select experimental data within this framework, demonstrates the significant potential of our approach. Future work will involve applying this efficient method to larger supercells incorporating Ge/Sb disorder to more accurately capture the properties of real-world PCM devices.

Methods

Structural models

Table 5 and Fig. 7 demonstrate the structural information of the six materials. Crystalline GST-225 has a hexagonal symmetry with space group $P\bar{3}m1$, whose basic repetitive stacking unit is Te-Ge-Te-Sb-Te-Te-Sb-Te-Ge, including 9 layers. The reference experimental lattice constants are

Table 4 | Number of atoms in a specific CN configuration per supercell, in several amorphous models

	CN	Number of atoms per supercell		
		Ge	Sb	Te
GST-147	1	0.1 (0.0)	1.8 (0.0)	3.6 (0.6)
	2	0.4 (0.0)	8.2 (0.5)	16.4 (54.3)
	3	2.7 (3.3)	11.8 (42.8)	49.2 (83.5)
	4	12.5 (14.4)	28.7 (37)	55.3 (19.7)
	5	5.5 (4.6)	27.8 (10.4)	29.4 (2.8)
	6	1.6 (1.0)	13.5 (1.4)	7.0 (0.0)
	7	0.1 (0.0)	0.2 (0.0)	0.2 (0.0)
	8	0.0 (0.0)	0.0 (0.0)	0.0 (0.0)
GST-124	CN	Ge	Sb	Te
	1	0.0 (0.0)	0.3 (0.0)	0.7 (0.3)
	2	0.2 (0.0)	1.5 (0.0)	13.2 (22.5)
	3	2.3 (13.4)	10.9 (2.8)	52.8 (71.2)
	4	17.7 (21)	24.7 (17.6)	61.2 (50.7)
	5	14.3 (4.6)	29.2 (33.6)	27.3 (13.3)
	6	5.5 (0.8)	13.2 (22.5)	4.7 (1.9)
	7	0.0 (0.0)	0.1 (3.2)	0.1 (0.0)
	8	0.0 (0.0)	0.0 (0.0)	0.0 (0.0)
GST-225	CN	Ge	Sb	Te
	1	0.1 (0)	0.1 (0.0)	1.4 (0.1)
	2	0.5 (0)	1.1 (0)	15.2 (29.6)
	3	3.5 (5.1)	7.5 (5.5)	54.5 (76.5)
	4	30.3 (31.3)	18.3 (19.6)	54.8 (38.3)
	5	19.5 (18.5)	22.1 (23.6)	21.2 (5.3)
	6	6.1 (4.7)	10.7 (11)	2.8 (0.2)
	7	0.0 (0.5)	0.1 (0.3)	0.1 (0.0)
	8	0.0 (0.0)	0.0 (0.0)	0.0 (0.0)
GST-326	CN	Ge	Sb	Te
	1	0.2 (0.0)	0.2 (0.0)	0.9 (0)
	2	0.8 (0.0)	0.6 (0.0)	10.3 (15.2)
	3	5.8 (6.1)	7.1 (2.4)	45.1 (68.4)
	4	37.7 (38.4)	16.7 (12.4)	62.6 (46.2)
	5	23.0 (24.5)	16.4 (18.8)	26.7 (15.7)
	6	7.6 (5.7)	8.7 (15)	4.3 (4)
	7	0.1 (0.2)	0.2 (1.4)	0.1 (0.3)
	8	0.0 (0.0)	0.0 (0.0)	0.0 (0.1)
Sb_2Te_3	CN	Ge	Sb	Te
	1	-	0.4 (0)	1.5 (0.2)
	2	-	2.1 (0)	18.9 (24.8)
	3	-	12.7 (8.1)	54.9 (84.1)
	4	-	32.9 (30)	62.5 (54.2)
	5	-	42.8 (45)	35.0 (15)
	6	-	28.8 (32.0)	7.0 (1.7)
	7	-	0.4 (4.6)	0.1 (0.1)
	8	-	0.0 (0.3)	0.0 (0.0)
	CN	Ge	Sb	Te
GeTe	1	0.7 (0.0)	-	2.5 (0.0)
	2	2.5 (0.0)	-	11.2 (17.5)
	3	10.7 (20.2)	-	53.3 (95.4)
	4	77.7 (86.1)	-	61.9 (33)
	5	43.1 (36.2)	-	18.9 (4)
	6	15.2 (7.3)	-	2.2 (0.1)
	7	0.1 (0.1)	-	0.0 (0.0)
	8	0.0 (0.0)	-	0.0 (0.0)

The value outside the parentheses was obtained through the MLAC method, while the value inside the parentheses was obtained through the traditional RDF integration method.

a = 4.25 Å, c = 18.27 Å[67], which are used for setting up the model cell. GST-124 is short of a Ge-Te bi-layer in its basic stacking unit compared with GST-225, i.e., Te-Ge-Te-Sb-Te-Te-Sb. To facilitate direct comparison with the experimental structural reports[67] and to clearly visualize the layered stacking sequences, we adopted the hexagonal setting for our structural models. In this setting, the conventional unit cell contains multiple formula units (e.g., 21 atoms for GST-124, 33 atoms for GST-326) to fulfill the periodicity requirements. But equivalent calculations could be performed using the smaller primitive trigonal cells. Hence, we set up a $1 \times 1 \times 3$ supercell that contains 21 layers, with initial lattice parameters of $a = 4.25$ Å, $c = 41.00$ Å[67]. The basic stacking unit of GST-326 contains Te-Ge-Te-Sb-Te-Te-Sb-Te-Ge-Te-Ge. It involves an additional Ge-Te bilayer compared to GST-225. Thus, a 33-layer model supercell was set up for GST-326, with initial lattice parameters $a = 4.25$ Å, $c = 62.60$ Å[67]. The basic stacking unit for GST-147 consists of Te-Sb-Te-Te-Sb-Te-Ge-Te-Sb-Te-Te-Sb, with 12 layers and $a = 4.236$ Å, $c = 23.761$ Å[68]. Matsunaga et al.[68] revealed a van der Waals-like weak force between Te and Te layers, as observed through X-ray diffraction and DFT calculations. However, a recent work by Kooi and Wuttig[69] suggests that in chalcogenide-based layered materials, the interlayer interactions may not be purely van der Waals in nature. Instead, these materials can exhibit metavalent bonding (MVB), a unique bonding mechanism characterized by a competition between electron delocalization and localization, which leads to stronger interlayer coupling than expected from typical van der Waals forces. This is particularly evident in compounds such as Sb_2Te_3, where the apparent van der Waals gap is smaller and shows enhanced interactions, serving as a fingerprint of MVB. While MVB implies a more complex bonding picture, we have incorporated van der Waals corrections in our DFT calculations to better describe the interlayer interactions, as this approach remains practical for capturing the non-covalent components in such systems. Sb_2Te_3 has a hexagonal lattice with space group $R\bar{3}m$, whose basic stacking unit is Te-Sb-Te-Te-Sb. To ensure that the number of layers along the c-axis is divisible by 3, a 15-layer supercell was established, with $a = 4.34$ Å, $c = 31.29$ Å[70]. At room temperature, GeTe also shows a hexagonal lattice with the $R3m$ space group. Its basic stacking unit contains merely Te-Ge, but the supercell has to contain 6 layers with $a = 4.23$ Å, $c = 10.92$ Å[70].

Density functional theory calculations

DFT calculations were performed with the Vienna Ab initio Simulation Package (VASP)[71,72], in terms of the projector augmented-wave[73,74] (PAW) method with a 350 eV plane-wave kinetic energy cutoff. The exchange-correlation energy was treated within the generalized gradient approximation using the PBE functional[16]. For the Ge pseudopotential, two common options include the standard 4-valance-electron (4e) Ge potential and the 14e Ge_d potential that includes semi-core 3d electrons. To make a justified choice, we conducted benchmark tests on GST-225 to evaluate both computational speed and accuracy. As detailed in Supplementary Note 7 and Supplementary Table 11, the results demonstrate that the two pseudopotentials yield very similar results, despite the difference in system sizes (48 electrons versus 68 electrons per unit cell). Therefore, the valence electron configurations were: 4s and 4p for Ge; 5s and 5p for Sb and Te. The van der Waals force correction was carried out using the DFT-D2 scheme by

Table 5 | Structural parameters and self-energy correction schemes

Material	Space group	Lattice constant (Å)				Exact way of shGGA-1/2
		a_0		c_0		
Sb_2Te_3	$R\bar{3}m$ (No. 166)	4.34[a]	4.26[b], 4.27[c], 4.34[i]	31.44[a]	30.45[b], 30.45[c], 31.29[i]	shGGA-1/4-1/4
GST-147	$P\bar{3}m1$ (No. 164)	4.23[a]	4.24[j]	24.05[a]	23.76[j]	shGGA-0-0-1/2
GST-124	$R\bar{3}m$ (No. 166)	4.23[a]	4.27[d], 4.25[h], 4.25[h]	41.26[a]	41.7[d], 41.0[h], 41.0[h]	shGGA-0-0-1/2
GST-225	$P\bar{3}m1$ (No. 164)	4.21[a]	4.22[e], 4.25[h]	17.16[a]	17.24[e], 18.27[h]	shGGA-0-0-1/2
GST-326	$R\bar{3}m$ (No. 166)	4.21[a]	4.21[f], 4.25[h]	61.76[a]	62.31[f], 62.6[h]	shGGA-0-0-1/2
GeTe	$R3m$ (No. 160)	4.23[a]	4.17[g], 4.23[k]	10.86[a]	10.62[g], 10.92[k]	shGGA-0-1/2

This table compiles the crystallographic parameters (space group and lattice constants) and the detailed self-energy correction schemes employed in the shGGA-1/2 calculations for all six investigated materials.
[a]The calculation result of our own.
[b]Experiment in ref. 82.
[c]Experiment in ref. 49.
[d]Experiment at 873 K in ref. 83.
[e]Experiment in ref. 55.
[f]Experiment at 90 K in ref. 84.
[g]Experiment in ref. 56.
[h]Experiment in ref. 67.
[i]Experiment in ref. 70.
[j]Experiment in ref. 68.

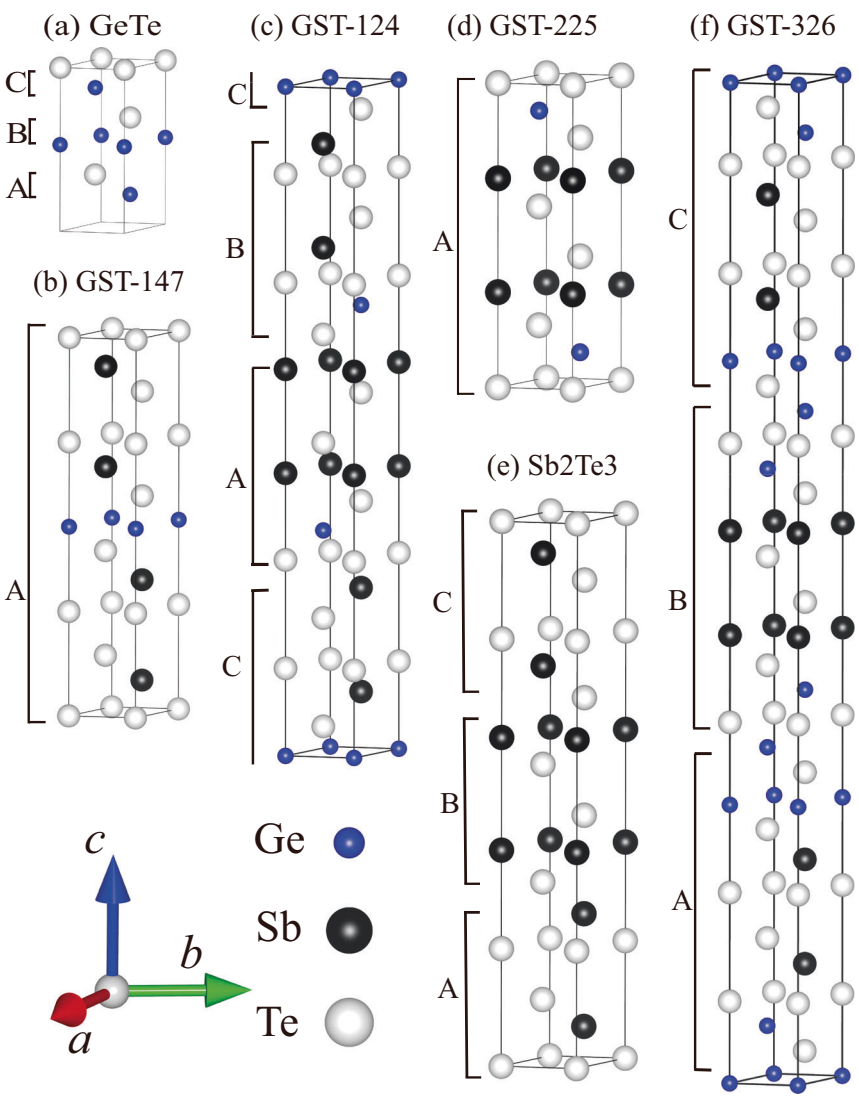

Fig. 7 | Crystal structures of GeTe and various GST compounds. a GeTe; **b** GST-147; **c** GST-124; **d** GST-225; **e** Sb_2Te_3; and **f** GST-326. Each symbol A, B, or C denotes a basic repetitive stacking unit of the structure along *c*-axis.

Grimme[75]. After constructing the initial models for the six materials, structure optimization was performed consistently using the PBE functional. Structural optimization criteria were: (i) the residual stress in any direction was less than 100 MPa; (ii) the Hellmann-Feynman force for any atom was below 0.005 eV/Å in any direction. In the structure optimization and self-consistent field (SCF) calculations, the equal-spacing Monkhorst-Pack scheme[76] was consistently used to generate the *k*-point grids. Following the structure optimization, band gap calculations were performed using various methods. Detailed *k*-point information and the calculation procedure can be found in Supplementary Note 1. The SCAN[45] and mBJ[46,47] functionals were used for the meta-GGA calculations, for comparative purposes.

After completing the structural optimization, to evaluate the structural stability and characteristics, we calculated the formation energies. First, we computed the energies of the three elemental substances (Ge, Sb, and Te), each in a 12 Å cubic cell containing only one atom. Subsequently, SCF calculations were performed to obtain the energies of these elements. For the six GST alloy materials, additional SCF calculations were carried out to determine their energies. The energy convergence criterion for the SCF calculations was set to 10^{-6} eV. The final formation energy results are presented in the Supplementary Table 12. The formation energies of all six GST alloys are negative, ranging from −3.621 to −3.871 eV/atom, showing their stability.

Optimization of self-energy potential cutoff radii in shell DFT-1/2

For electronic structure calculations, all DFT-1/2-type methods attach the self-energy potentials to the anions, which account for a majority part of the valence band states. In shell DFT-1/2, a shell-like trimming function is used to confine the spatial range of the self-energy potential, defined as:

$$\Theta(r)=\begin{Bmatrix} 0 & r<r_{in} \\ \left\{1-\left[\frac{2(r-r_{in})}{r_{out}-r_{in}}-1\right]^{p}\right\}^{3} & r_{in}\le r\le r_{out} \\ 0 & r>r_{out} \end{Bmatrix} \quad (1)$$

where the power index p is an even integer, which should be sufficiently large and is recommended to be $p = 20$. Here, r_{in} and r_{out} denote the inner and outer radii of the cutoff function, respectively. Both values ought to be obtained from the variational principle, to maximize the band gap. This is because shell DFT-1/2 pulls down the valence band of the semiconductor or insulator, through rectifying the spurious electron self-interaction error. To recover the ground state from an ionized state, the total energy should be minimized, thus the band gap ought to be maximized. In this sense, the cutoff radii r_{in} and r_{out} should not be regarded as parameters in shell DFT-1/2, because they are derived computationally, not empirically. After trimming, the self-energy potential is attached to the pseudopotentials of the anions for the self-energy correction for the valence band. In other words, the self-energy corrected pseudopotentials are used in standard self-consistent electronic structure calculations[30,35]. For highly ionic compounds it is straightforward to identify the anion elements. However, the bonding in PCMs is different from that of a typical ionic bond. Hence, we adopted the differential charge method to explore the spatial extension of valence band holes. This involves subtracting 0.01 electron from a unit cell and comparing the charge distribution between the neutral cell and that of the ionized cell. The reason for using 0.01 electron instead of one electron lies in that this does not perturb the electronic states to an undesirable extent. The differential charge density will then be magnified by 100 times to recover one electron removal[33]. The hole locations are illustrated in Supplementary Fig. 1. It seems that for GeTe one should prefer shGGA-0-1/2, where 0 and 1/2 are the amounts of equivalent electron removal from Ge and Te, respectively. For Sb_2Te_3, on the other hand, shGGA-1/4-1/4 is to be carried out, where Sb and Te are both subject to 1/4 electron removal. The various GST models (GST-147, GST-124, GST-225, GST-326) fit shGGA-0-0-1/2, where 0, 0 and 1/2 are the amounts of equivalent electron removal from Ge, Sb, and Te, respectively. Through scanning r_{in} and r_{out} to maximize the band gaps, all cutoff radii are obtained unambiguously as listed in Table 6. Since near the extreme point, the band gap varies very slowly with respect to the cutoff radii, it turns out that a consistent setting Te $r_{in} = 0.9$ Bohr and Te $r_{out} = 3.0$ Bohr can be used for GST in general, though in GST-326 we used the optimal value $r_{out} = 2.9$ Bohr, which makes extremely little difference.

Table 6 | The optimized self-energy potential cutoff radii for the six materials under shell GGA-1/2 calculations

	Radius (Bohr)					
	Sb_2Te_3	GST-147	GST-124	GST-225	GST-326	GeTe
r_{in}	Sb: 0.1	Te: 0.8	Te: 0.9	Te: 0.9	Te: 0.9	Te: 0.8
	Te: 1.2					
r_{out}	Sb: 1.6	Te: 3.0	Te: 3.0	Te: 3.0	Te: 2.9	Te: 3.0
	Te: 3.4					

Ab initio molecular dynamics

A melt-quench scheme[77] was employed to generate the amorphous structures of Sb_2Te_3 (a-Sb_2Te_3), amorphous GST (a-GST-147, a-GST-124, a-GST-225 as well as a-GST-326), and amorphous GeTe (a-GeTe). AIMD simulation was performed within the Born–Oppenheimer framework[78] as implemented in VASP. The canonical NVT ensemble was used with a Langevin thermostat[79]. The time step was set to 2 fs, and only the Γ point was used to sample the Brillouin zone of all models. All model supercells were first melted at a high temperature of 2000 K for 20 ps. Subsequently, during the quenching process, the temperature was gradually reduced to 300 K. The size of the simulation box was adjusted multiple times, to minimize internal stress. The quenching time for each structure was 50 ps, with a cooling rate of approximately 34 K/ps. After cooling to 300 K, the system was equilibrated at this temperature for 10 ps to ensure thermal stability. The resulting amorphous structures underwent thorough geometric relaxation to further reduce internal stress, ensuring that the absolute value of the final stress in all models was less than 100 MPa.

Data availability

The datasets that support the findings of this study are available from the corresponding author upon reasonable request.The underlying code is available from the corresponding author upon reasonable request.

Code availability

The underlying code is available from the corresponding author upon reasonable request.

Received: 29 July 2025; Accepted: 9 December 2025;
Published online: 29 December 2025

References

1. Wuttig, M. & Yamada, N. Phase-change materials for rewriteable data storage. *Nat. Mater.* **6**, 824–832 (2007).
2. Zhang, W., Mazzarello, R., Wuttig, M. & Ma, E. Designing crystallization in phase-change materials for universal memory and neuro-inspired computing. *Nat. Rev. Mater.* **4**, 150–168 (2019).
3. Wang, Z. et al. Resistive switching materials for information processing. *Nat. Rev. Mater.* **5**, 173–195 (2020).
4. Sun, L. et al. Ab initio molecular dynamics and materials design for embedded phase-change memory. *npj Comput. Mater.* **7**, 1–8 (2021).
5. Abou El Kheir, O., Bonati, L., Parrinello, M. & Bernasconi, M. Unraveling the crystallization kinetics of the $Ge_2Sb_2Te_5$ phase change compound with a machine-learned interatomic potential. *npj Comput. Mater.* **10**, 33 (2024).
6. Wang, W. H., Chung, L. C. & Kuo, C. T. Effects of the Sb_2Te_3 crystallization-induced layer on crystallization behaviors and

properties of phase change optical disk. *Surf. Coat. Technol.* **177-178**, 795–799 (2004).
7. Medvedev, M. G., Bushmarinov, I. S., Sun, J., Perdew, J. P. & Lyssenko, K. A. Density functional theory is straying from the path toward the exact functional. *Science* **365**, 49–52 (2017).
8. Hohenberg, P. & Kohn, W. Inhomogeneous electron gas. *Phys. Rev.* **136**, B864–B871 (1964).
9. Lee, G. & Jhi, S.-H. Ab initio studies of structural and electronic properties of the crystalline $Ge_2Sb_2Te_5$. *Phys. Rev. B* **77**, 153201 (2008).
10. Yamanaka, S., Ogawa, S., Morimoto, I. & Ueshima, Y. Electronic structures and optical properties of GeTe and $Ge_2Sb_2Te_5$. *Jpn. J. Appl. Phys.* **37**, 3327 (1998).
11. Park, J.-W., Eom, S. H. & Lee, H. Optical properties of pseudobinary GeTe, $Ge_2Sb_2Te_5$, $GeSb_2Te_4$, $GeSb_4Te_7$, and Sb_2Te_3 from ellipsometry and density functional theory. *Phys. Rev. B* **80**, 115209 (2009).
12. Ibarra-Hern ndez, W. & Raty, J.-Y. Ab initio density functional theory study of the electronic, dynamic, and thermoelectric properties of the crystalline pseudobinary chalcogenide $(GeTe)_x/(Sb_2Te_3)$ (x = 1, 2, 3). *Phys. Rev. B* **97**, 245205 (2018).
13. Ceperley, D. M. & Alder, B. J. Ground state of the electron gas by a stochastic method. *Phys. Rev. Lett.* **45**, 566–569 (1980).
14. Kohn, W. & Sham, L. J. Self-consistent equations including exchange and correlation effects. *Phys. Rev.* **140**, A1133–A1138 (1965).
15. Becke, A. D. Density-functional thermochemistry. I. The effect of the exchange-only gradient correction. *J. Chem. Phys.* **96**, 2155–2160 (1992).
16. Perdew, J. P., Burke, K. & Ernzerhof, M. Generalized gradient approximation made simple. *Phys. Rev. Lett.* **77**, 3865–3868 (1996).
17. Perdew, J. P. et al. Atoms, molecules, solids, and surfaces: applications of the generalized gradient approximation for exchange and correlation. *Phys. Rev. B.* **46**, 6671 (1992).
18. Lee, C., Yang, W. & Parr, R. G. Development of the Colle-Salvetti correlation-energy formula into a functional of the electron density. *Phys. Rev. B* **37**, 785–789 (1988).
19. Becke, A. D. Density-functional thermochemistry. III. The role of exact exchange. *J. Chem. Phys.* **98**, 5648–5652 (1993).
20. Heyd, J., Scuseria, G. E. & Ernzerhof, M. Hybrid functionals based on a screened Coulomb potential. *J. Chem. Phys.* **118**, 8207–8215 (2003).
21. García-González, P. & Godby, R. W. Self-consistent calculation of total energies of the electron gas using many-body perturbation theory. *Phys. Rev. B* **63**, 075112 (2001).
22. Hedin, L. New method for calculating the one-particle Green's function with application to the electron-gas problem. *Phys. Rev.* **139**, A796–A823 (1965).
23. Aryasetiawan, F. & Gunnarsson, O. The *GW* method. *Rep. Prog. Phys.* **61**, 237 (1998).
24. Dragoni, D., Gabardi, S. & Bernasconi, M. First-principles study of the liquid and amorphous phases of In_2Te_3. *Phys. Rev. Mater.* **1**, 035603 (2017).
25. Zhang, W., Wuttig, M. & Mazzarello, R. Effects of stoichiometry on the transport properties of crystalline phase-change materials. *Sci. Rep.* **5**, 13496 (2015).
26. Zipoli, F., Krebs, D. & Curioni, A. Structural origin of resistance drift in amorphous GeTe. *Phys. Rev. B* **93**, 115201 (2016).
27. Kim, K. Y. et al. Competing local orders in liquid and amorphous structures of $Ge_2Sb_2Te_5$: Influence of exchange-correlation functional. *J. Appl. Phys.* **113**, 134302 (2013).
28. Su, J. et al. Theoretical predictions of the structural stability and property contrast for Sb-rich $Ge_3Sb_6Te_5$ phase-change materials. *Appl. Phys. Lett.* **122**, 252102 (2023).
29. Lee, T. H. & Elliott, S. R. The relation between chemical bonding and ultrafast crystal growth. *Adv. Mater.* **29**, 1700814 (2017).
30. Mao, G.-Q. et al. DFT-1/2 and shell DFT-1/2 methods: Electronic structure calculation for semiconductors at LDA complexity. *J. Phys. Condens. Matter* **34**, 403001 (2022).
31. Ferreira, L. G., Marques, M. & Teles, L. K. Approximation to density functional theory for the calculation of band gaps of semiconductors. *Phys. Rev. B* **78**, 125116 (2008).
32. Ferreira, L. G., Marques, M. & Teles, L. K. Slater half-occupation technique revisited: The LDA-1/2 and GGA-1/2 approaches for atomic ionization energies and band gaps in semiconductors. *AIP Adv.* **1**, 032119 (2011).
33. Xue, K.-H., Yuan, J.-H., Fonseca, L. R. C. & Miao, X.-S. Improved LDA-1/2 method for band structure calculations in covalent semiconductors. *Comput. Mater. Sci.* **153**, 493–505 (2018).
34. Cui, H. et al. Shell DFT-1/2 method towards engineering accuracy for semiconductors: GGA versus LDA. *Comput. Mater. Sci.* **213**, 111669 (2022).
35. Cui, H., Yang, S., Xue, K.-H., Huang, J. & Miao, X. On the self-consistency of DFT-1/2. *J. Chem. Phys.* **158**, 094103 (2023).
36. Ai, Z et al. DFT-1/2 for ionic insulators: Impact of self-energy potential on band gap correction. *Comput. Mater. Sci.* **239**, 112978 (2024).
37. Yang, S. et al. Enabling ab initio material design of InAs/GaSb superlattices for infrared detection. *Phys. Rev. Appl.* **18**, 024058 (2022).
38. Feng, N. et al. Anti-Jahn-Teller effect induced ultrafast insulator to metal transition in perovskite $BaBiO_3$. *npj Comput. Mater.* **8**, 226 (2022).
39. Yuan, J.-H. et al. GGA-1/2 self-energy correction for accurate band structure calculations: The case of resistive switching oxides. *J. Phys. Commun.* **2**, 105005 (2018).
40. Lawal, A. & Shaari, A. Density functional theory study of electronic properties of Bi_2Se_3 and Bi_2Te_3. *Mal. J. Fund. Appl. Sci.* **12**, 6671 (2017).
41. Hsieh, D. et al. Observation of time-reversal-protected single-Dirac-cone topological-insulator states in Bi_2Te_3 and Sb_2Te_3. *Phys. Rev. Lett.* **103**, 146401 (2009).
42. Perdew, J. P. et al. Restoring the density-gradient expansion for exchange in solids and surfaces. *Phys. Rev. Lett.* **100**, 136406 (2008).
43. Heyd, J., Scuseria, G. E. & Ernzerhof, M. Hybrid functionals based on a screened Coulomb potential. *J. Chem. Phys.* **124**, 219906 (2006).
44. Krukau, A. V., Vydrov, O. A., Izmaylov, A. F. & Scuseria, G. E. Influence of the exchange screening parameter on the performance of screened hybrid functionals. *J. Chem. Phys.* **125**, 224106 (2006).
45. Sun, J., Ruzsinszky, A. & Perdew, J. P. Strongly constrained and appropriately normed semilocal density functional. *Phys. Rev. Lett.* **115**, 036402 (2015).
46. Becke, A. D. & Johnson, E. R. A simple effective potential for exchange. *J. Chem. Phys.* **124**, 221101 (2006).
47. Tran, F. & Blaha, P. Accurate band gaps of semiconductors and insulators with a semilocal exchange-correlation potential. *Phys. Rev. Lett.* **102**, 226401 (2009).
48. Yuan, J.-H. et al. Ferroelectricity in HfO_2 from a coordination number perspective. *Chem. Mater.* **35**, 94–103 (2023).
49. Lawal, A., Shaari, A., Ahmed, R. & Jarkoni, N. Sb_2Te_3 crystal a potential absorber material for broadband photodetector: A first-principles study. *Results Phys.* **7**, 2302–2310 (2017).
50. Huang, B. & Robertson, J. Nature of defects and gap states in GeTe model phase change materials. *Phys. Rev. B* **85**, 125305 (2012).
51. Wu, D., Xie, L., Xu, X. & He, J. High thermoelectric performance achieved in GeTe-Bi_2Te_3 pseudo-binary via Van der Waals gap-induced hierarchical ferroelectric domain structure. *Adv. Funct. Mater.* **29**, 1806613 (2019).
52. Sosso, G. C., Caravati, S. & Bernasconi, M. Vibrational properties of crystalline Sb_2Te_3 from first principles. *J. Phys. Condens. Matter* **21**, 095410 (2009).
53. Kolobov, A. V. et al. Why phase-change media are fast and stable: A new approach to an old problem. *Jpn. J. Appl. Phys.* **44**, 3345 (2005).
54. Makino, K., Tominaga, J., Kolobov, A. V., Fons, P. & Hase, M. Bond-selective excitation and following displacement of Ge atoms in GeTe/Sb_2Te_3 superlattice. *Acta Phys. Pol. A* **121**, 336–339 (2012).
55. Matsunaga, T., Yamada, N. & Kubota, Y. Structures of stable and metastable $Ge_2Sb_2Te_5$, an intermetallic compound in GeTe-Sb_2Te_3

pseudobinary systems. *Acta Crystallogr. B Struct. Sci.* **60**, 685–691 (2004).
56. Nonaka, T., Ohbayashi, G., Toriumi, Y., Mori, Y. & Hashimoto, H. Crystal structure of GeTe and $Ge_2Sb_2Te_5$ meta-stable phase. *Thin Solid Films* **370**, 258–261 (2000).
57. Yamada, N. & Matsunaga, T. Structure of laser-crystallized $Ge_2Sb_{2+x}Te_5$ sputtered thin films for use in optical memory. *J. Appl. Phys.* **88**, 7020–7028 (2000).
58. Njoroge, W. K. et al. Density changes upon crystallization of $Ge_2Sb_{2.04}Te_{4.74}$ films. *J. Vac. Sci. Technol. A* **20**, 230–233 (2002).
59. Wu, R. et al. The role of arsenic in the operation of sulfur-based electrical threshold switches. *Nat. Commun.* **14**, 6095 (2023).
60. Akola, J. & Jones, R. O. Structural phase transitions on the nanoscale: The crucial pattern in the phase-change materials $Ge_2Sb_2Te_5$ and GeTe. *Phys. Rev. B* **76**, 235201 (2007).
61. Konstantinou, K., Mocanu, F. C., Lee, T.-H. & Elliott, S. R. Revealing the intrinsic nature of the mid-gap defects in amorphous $Ge_2Sb_2Te_5$. *Nat. Commun.* **10**, 3065 (2019).
62. Clima, S. et al. Ovonic threshold switch chalcogenides: Connecting the first-principles electronic structure to selector device parameters. *ACS Appl. Electron. Mater.* **5**, 461–469 (2023).
63. Kato, T. & Tanaka, K. Electronic properties of amorphous and crystalline $Ge_2Sb_2Te_5$ films. *Jpn. J. Appl. Phys.* **44**, 7340 (2005).
64. Kolobov, A. V. & Tanaka, K. Photoinduced phenomena in amorphous chalcogenides: From phenomenology to nanoscale. in *Handbook of Advanced Electronic and Photonic Materials and Devices* (ed. Singh Nalwa, H.) 47–90. https://doi.org/10.1016/B978-012513745-4/50043-3 (Academic Press, Burlington, 2001).
65. Kim, J. & Jhi, S.-H. Disorder-induced structural transitions in topological insulating Ge-Sb-Te compounds. *J. Appl. Phys.* **117**, 195701 (2015).
66. Matsunaga, T., Yamada, N. & Kubota, Y. Structures of stable and metastable $Ge_2Sb_2Te_5$, an intermetallic compound in GeTe-Sb_2Te_3 pseudobinary systems. *Acta Cryst. B* **60**, 685–691 (2004).
67. Kooi, B. J. & De Hosson, J. T. M. Electron diffraction and high-resolution transmission electron microscopy of the high temperature crystal structures of $Ge_xSb_2Te_{3+x}$ (x=1,2,3) phase change material. *J. Appl. Phys.* **92**, 3584–3590 (2002).
68. Matsunaga, T. et al. Structural features of $Ge_1Sb_4Te_7$, an intermetallic compound in the GeTe-Sb_2Te_3 homologous series. *Chem. Mater.* **20**, 5750–5755 (2008).
69. Kooi, B. J. & Wuttig, M. Chalcogenides by design: functionality through metavalent bonding and confinement. *Adv. Mater.* **32**, 1908302 (2020).
70. Da Silva, J. L. F., Walsh, A. & Lee, H. Insights into the structure of the stable and metastable $(GeTe)_m(Sb_2Te_3)_n$ compounds. *Phys. Rev. B* **78**, 224111 (2008).
71. Kresse, G. & Furthmüller, J. Efficiency of ab-initio total energy calculations for metals and semiconductors using a plane-wave basis set. *Comput. Mater. Sci.* **6**, 15–50 (1996).
72. Kresse, G. & Furthmüller, J. Efficient iterative schemes for ab initio total-energy calculations using a plane-wave basis set. *Phys. Rev. B* **54**, 11169–11186 (1996).
73. Blöchl, P. E. Projector augmented-wave method. *Phys. Rev. B* **50**, 17953–17979 (1994).
74. Kresse, G. & Joubert, D. From ultrasoft pseudopotentials to the projector augmented-wave method. *Phys. Rev. B* **59**, 1758–1775 (1999).
75. Grimme, S. Semiempirical GGA-type density functional constructed with a long-range dispersion correction. *J. Comput. Chem.* **27**, 1787–1799 (2006).
76. Monkhorst, H. J. & Pack, J. D. Special points for Brillouin-zone integrations. *Phys. Rev. B* **13**, 5188–5192 (1976).
77. Zhang, W. et al. Density-functional theory guided advances in phase-change materials and memories. *MRS Bull.* **40**, 856–869 (2015).
78. Born, M. & Oppenheimer, R. Zur Quantentheorie der Molekeln. *Ann. der Phys.* **389**, 457–484 (1927).
79. Kühne, T. D., Krack, M., Mohamed, F. R. & Parrinello, M. Efficient and accurate Car-Parrinello-like approach to Born-Oppenheimer molecular dynamics. *Phys. Rev. Lett.* **98**, 066401 (2007).
80. Olson, J. K., Li, H., Ju, T., Viner, J. M. & Taylor, P. C. Optical properties of amorphous GeTe, Sb_2Te_3, and $Ge_2Sb_2Te_5$: The role of oxygen. *J. Appl. Phys.* **99**, 103508 (2006).
81. Lee, B.-S. et al. Investigation of the optical and electronic properties of $Ge_2Sb_2Te_5$ phase change material in its amorphous, cubic, and hexagonal phases. *J. Appl. Phys.* **97**, 093509 (2005).
82. Villars, P. & Calvert, L. D. *Pearson's Handbook of Crystallographic Data for Intermetallic Phases*. (ASM International, Materials Park, 1991).
83. Matsunaga, T. & Yamada, N. Structural investigation of $GeSb_2Te_4$: A high-speed phase-change material. *Phys. Rev. B* **69**, 104111 (2004).
84. Matsunaga, T. et al. Structural investigation of $Ge_3Sb_2Te_6$, an intermetallic compound in the GeTe-Sb_2Te_3 homologous series. *Appl. Phys. Lett.* **90**, 161919 (2007).

Acknowledgements

This work was supported by the National Science and Technology Major Project of China (Grant No. 2022ZD0117600) and the National Natural Science Foundation of China under Grant No. 12474230.

Author contributions

K.-H.X. and M.X. jointly conceived the idea; K.-H.X. and X.S.M. supervised the work. S.Z.X. performed the DFT calculations with assistance from Z.J.Z., S.X.Y., and H.Y.; S.Z.X. constructed the models and conducted coordination number analysis with the assistance from S.J.Y. and R.C.G.; The manuscript was written by K.-H.X., M.X., and S.Z.X., and was revised based on feedbacks from all authors.

Competing interests

The authors declare no competing interests.

Additional information

Supplementary information The online version contains supplementary material available at https://doi.org/10.1038/s41524-025-01922-w.

Correspondence and requests for materials should be addressed to Kan-Hao Xue or Ming Xu.